Supplementary Information for "*Coacervate or precipitate?* Formation of non-equilibrium microstructures in coacervate emulsions"

Chelsea E.R. Edwards, Kareem L. Lakkis, Yimin Luo, and Matthew E. Helgeson

October 7, 2023

Note 1   PAA-PAH Phase Space

Thermogravimetric Analysis (TGA) data collected by Luo et al. provides experimentally-determined dense and dilute phase boundaries for the PAA-PAH system up to the highest salt compositions in literature to date.[1] Note that we prepared PAA-PAH coacervates using the same molecular weights and supplier as the work by Luo et al., so these phase boundaries describe the system herein. Hence, Luo's data is used in Figure S1. For easy comparison to experiments herein, y-axis data have been transformed to the total (as-prepared) system NaCl concentration, resulting in artificially horizontal tie lines; plotting salt volume fraction (commonly denoted Ψ) on the ordinate would reveal the PAA-PAH system's negatively-sloped tie lines. The phase boundaries in Ψ vs. Φ, polymer volume fraction, are available in Luo's paper,[1] and are consistent in the lower salt regime with the coacervate phase behavior of the PAA-PAH chemistry as studied by others.[2, 3, 4, 5]
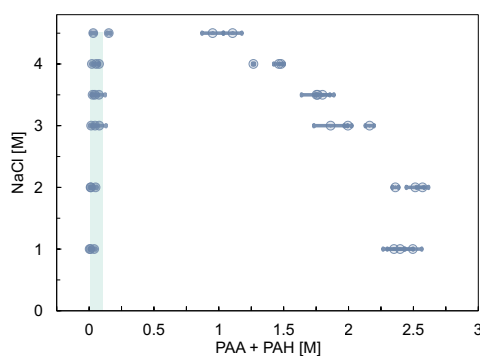

Figure S1: The range of salt and polymer preparation compositions tested in this work (light blue box) relative to the equilibrium dense and dilute phase compositions (dark blue points) for the PAA-PAH system of the same chain lengths and pH (6.5) *via* Luo et al.[1]

Note 2   Manufacturing μfluidic Chips from 3D-Printed Molds

Negative masters are 3D-printed from SOLIDWORKS® Y-junction designs using a MiiCraft 125 series 3D-printer and the MiiCraft proprietary photopolymer resin BV007. The print is followed by a 10 minute wash in isopropanol and a 10 minute additional cure in a UV chamber. Finally, it is baked in the oven at 130°C for 4 hours. These additional steps ensure that the resin surface is free from unreacted functional groups in the resin that were found to inhibit PDMS polymerization.

Since the additional cure in the oven can affect printed dimensions, accuracy of the dimensions after the post-treatment process is corroborated to within a 1% variation across chips at least 5 points along the

mixing channel using a Keyence VHX-5000 digital microscope. Unsatisfactory molds are discarded, and satisfactory ones are treated with silane via vapor deposition for 30 minutes prior to use.

Soft lithography protocol is as follows. The SYLGARD® 184 Silicone Elastomer base and curing agent were mixed in a 10:1 ratio by weight. The components are mixed and defoamed for 30 seconds in an automated mixer, poured onto the molds. The elastomer mix was degassed four times for 7 minutes each, popping bubbles with a gentle nitrogen stream between evacuations. The mixture is heat cured at 65°C for 30-40 minutes. The resulting PDMS replicas are cut away from the negative masters with an X-Acto knife. Holes are bored through the PDMS replicas at the Y-junction inlets and outlet with a 1.5 mm punch to match the tubing OD (1.52 mm). Each PDMS replica and a corresponding a glass microscope slides were washed well with acetone and isopropanol for at least 5 minutes, dried with a nitrogen stream, and placed into an ozone chamber for 10 minutes for surface activation. PDMS replicas were manually bonded to the treated glass slides, and these final devices were cured overnight at 60°C to ensure bonding.
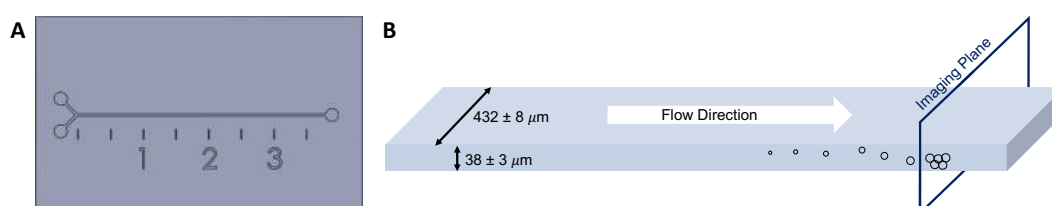
Note 2.1   Mixing channel geometry

Figure S2: Microfluidic channel geometry in the mixing region of the Y-junction device. Panel A shows the top view of the CAD design for the device, with centimeter lengths down the mixing channel marked. Panel B shows a schematic of the side view of the mixing region after soft lithography (not to scale), with an example imaging plane used to take time series images of droplets or growing sediment.

Note 3   Droplet Growth

Note 3.1   Drop sizing in microfluidics

To monitor formation of coacervate droplets and precipitate particles during microfluidic mixng, droplet radii are extracted from snapshots of microscopy videos at constantly-spaced axial positions (mixing channel length l). Counting many video frames per l enables statistically meaningful size distributions to be extracted. Videos are collected at a frame rate (10 Hz) chosen so as not to capture droplets on multiple video frames for the 40x objective, and 1.6 optical zoom settings used to collect the kinetics data discussed in this section. Example snapshots are shown in Figure S3.
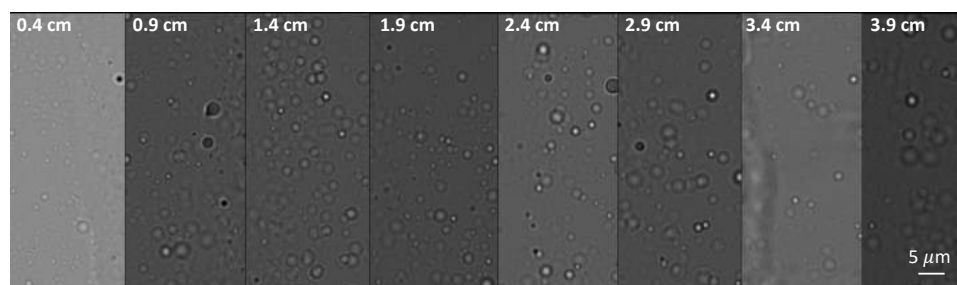

Figure S3: Example snapshots from videos of PEC droplets formed at various channel lengths during mixing of PAA and PAH at 30 mM r.u. and 4.5 M NaCl at 0.5 μL/min.

Assuming the droplets move at the average linear velocity u, the average space-time τ of a droplet for some l is $\tau = \dfrac{l}{u}$. This is a rough approximation due to differences between streamlines, as well as various

forces experienced by PEC droplets once they form, like sedimentation, drag, and lift. Regardless, measurement of droplet distribution at a given space-time τ can be used to quantify growth rate.

An image processing algorithm was built to extract droplet volume distribution and volume-averaged radius $\langle R \rangle$ at each l. Obtaining droplet sizes from the videos is not straightforward, since image processing must only retain in-focus, flowing droplets, and discard those at other focal planes or sedimented on the channel floor and ceiling. To avoid counting sedimented droplets, videos were background-subtracted by subtracting the average video intensity at every pixel in each frame. A custom-developed procedure was then used to identify flowing droplets that were in the focal plane and calculate their individual radii. Droplet detection uses a combination of thresholding, circularity calculation, and detection of high gradients (Figure S4). In particular, each image was quantized into a three-level thresholded image (threshold values computed using the Otsu method via MATLAB's built-in "multithresh" function) to separate in-focus droplets (light) from background (medium) and droplet outlines/out-of-focus drops (dark). MATLAB's "bwconncomp" function was used to catalog the various properties of each light connected region, and those with circularity > 0.5 and whose area did not exceed 20 μm (as an arbitrary, overestimated upper-bound) were stored as test regions. Next, a second set of test regions were generated to compare with the first. Because in-focus droplets had high gradients at their edge compared to out-of-focus droplets, an edge-detection algorithm was run on the original image (MATLAB's "edge" using a Laplacian of Gaussian filter with threshold 0.005) to identify connected droplet outlines. The centers and diameters of these connected regions were calculated to form the second set. Regions were discarded from the set if their perimeter did not exceed 5 pixels, or if—comparing to the three-level thresholded version of the image—the region was not bounded by a "dark" above/below and to the left/right at the same radial distance from the center (a secondary method of ensuring circularity, and that the direction of the high gradient corresponded to in-focus droplets). Droplets that are found in both test sets were counted and considered to be in-focus droplets.

This procedure is extremely selective in that very few possible droplets pass through both test sets. The algorithm should only find in-focus droplets, because only droplets with both large gradients from bright-to-dark in a circular pattern are counted. Using these strict criteria, over many video frames (at least 20), a statistical distribution of drop sizes was obtained. A slow frame rate of 1 s was used so that the same droplets did not appear twice in successive frames.
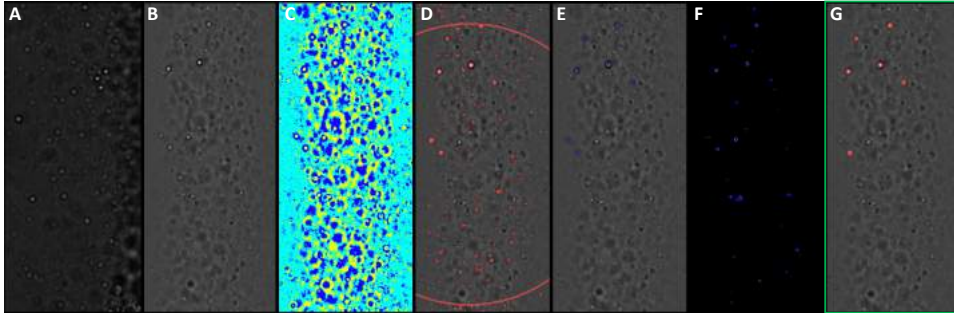

Figure S4: Image processing to find only the in-focus droplets in each video frame. (a) Raw image. (b) Background subtraction. (c) Three-level thresholding. (d) Connected, bright regions from (c) are fit to circles. (e) Circles with reasonable area and circularity. (f) Locations of connected, high-gradient regions in (b). (g) Test droplets found in (e) and (f) are compared, and those found from both are kept, resulting in the final set of in-focus droplets for this video frame (red circles). Scale bar matches Figure S3.

The set of radii detected from all video frames taken at each l gives a direct measurement of the droplet size distribution for that l. Droplet distributions are lognormal and broaden with increasing channel length, developing a larger positive-skewed tail (Figure S5A). A cumulative distribution function (CDF) can be constructed the from the volume distributions at each l and fit to the lognormal CDF,

$$\frac{1}{2}\left(1 + \text{erf}\left[\frac{ln(x) - \mu}{\sigma\sqrt{2}}\right]\right)$$

as shown in Figure S5B. This fit gives the volume-average radius, $\mu = \langle R \rangle$, and variance, σ, of the lognormal distribution for that l and τ. Since mixing has just begun at $\tau = l = 0$, it is assumed that

$\langle R \rangle = 0$. The resulting τ versus $\langle R \rangle$ plot (Figure S5C) reveal the coacervate droplet growth kinetics, and can be analyzed for concentrations across salt-polymer space as discussed in Section 2.2.1.
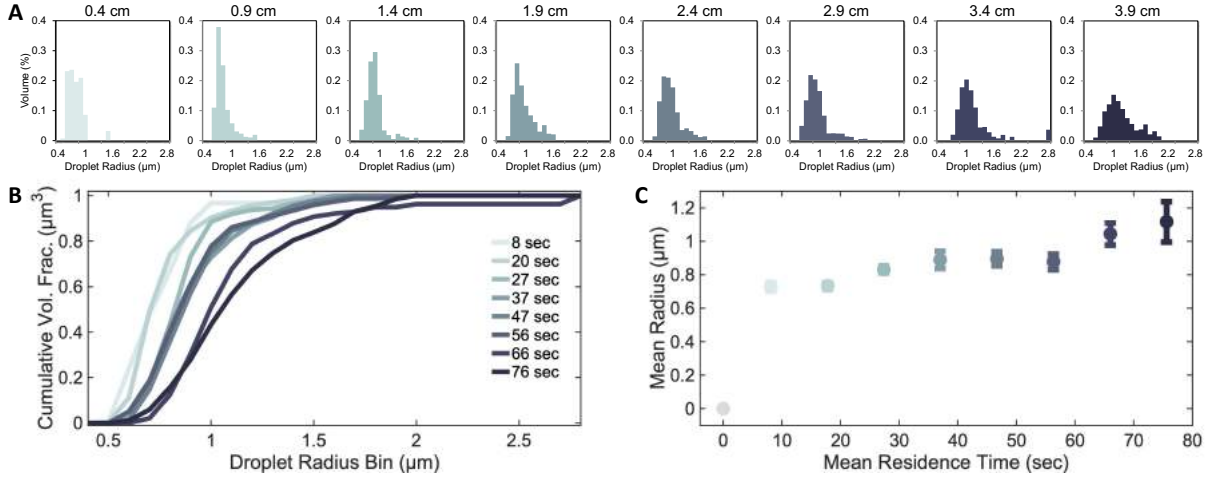

Figure S5: Sample droplet volume distributions and associated CDF fits to find mean radii. Data shown for the 30 mM r.u. and 4.5 M NaCl system at 0.5 μL/min flow rate. (a) Droplet volume distributions at increasing channel lengths and corresponding space-times: $l = 0.4$ cm, τ 8 s; $l = 0.9$ cm, τ 20 s; $l = 1.4$ cm, τ 27 s; $l = 1.9$ cm, τ 37 s; $l = 2.4$ cm, τ 47 s; $l = 2.9$ cm, τ 56 s; $l = 3.4$ cm, τ 66 s; and $l = 3.4$ cm, τ 76 s. (b) CDFs of the associated volume distributions. (c) CDF means and variance give the increasing volume-averaged radius $\langle R \rangle$ and standard deviation at each τ. The light gray point at (0,0) is not measured but rather necessarily 0 since $\tau = 0$ at the beginning of the channel.

Note 3.2   Growth past diffraction limit

A linear fit of the channel length corresponding to the first visible droplets, l_o, versus volumetric flow rate (Q) gives an estimated timescale for initial droplet growth as $average\left[A\left(\dfrac{\Delta l_o}{\Delta Q}\right)\right]$, where A is the cross-section of the microfluidic channel (A = 16074 μm^2). A linear fit assumes that initial growth is not significantly affected by shear or velocity; however, the R^2 = 0.984, suggesting that this assumption holds over the tested Q-range.
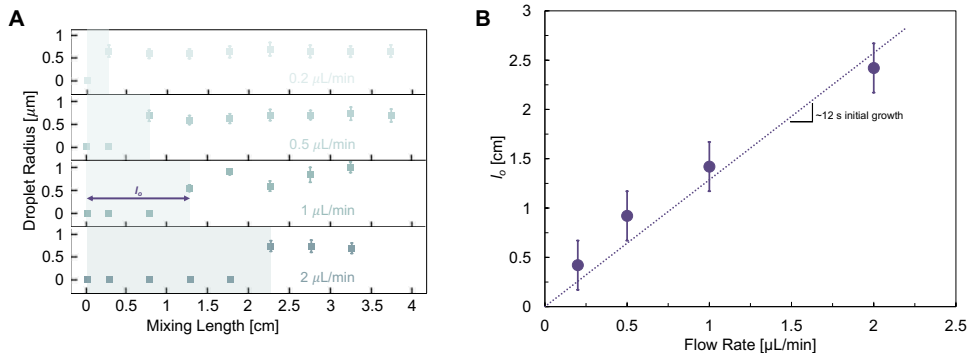

Figure S6: Initial Growth Rate Fit Example. (A) Average PEC droplet size is quantified at various channel lengths and flow rates, remaining near 1 μm once visible droplets form at length l_o(10 mM r.u. and 4.5 M NaCl). (B) A linear fit of l_o—the mixing channel length corresponding to the apparent drop size jump—vs. Q gives an estimated timescale for initial droplet growth of 12 seconds for the 10 mM r.u. and 4.5 M NaCl system; l_o were extracted from (A).

Note 3.3   Droplet coarsening *via* DLS

Dynamic Light Scattering (DLS) was used to monitor coacervate size for the first 600 s of growth to assess the rate of droplet growth after the initial fast stage. Stock solutions were passed through a 0.45 μ m Teflon syringe filter prior to measurement to minimize dust contamination, and then mixed into a glass sample tube according to the vortex mixing protocol immediately prior to measurement.

DLS measurements were performed using a Brookhaven Instruments 200SM multiangle detector system, equipped with a Cobolt Samba 500 mW continuous-wave diode-pumped laser (λ = 532 nm). Laser intensity was modulated using a neutral density filter (1, 10, 20, 50, or 100% transparency) and pinhole size chosen such that the average count rate during measurement remained within 150-500 kcps. Measurements were performed at a fixed detector angle of 90°and maintained at room temperature (25°C ±0.5°C) by an ethylene glycol/water bath circulator. An autocorrelation function was collected every 30 seconds, and the hydrodynamic radius and standard deviation were determined using the method of cumulants, with parameters for pure water at 25°C.

The resulting growth rates measured by DLS are of similar magnitude as those observed on-chip, despite differences in the flow history between these approaches, and the DLS fit is considered to more accurately describe longer-time coarsening because of the longer duration for data collection. The slower apparent growth rate is linear in $\langle R\rangle^3$ versus time after vortexing (Figure S7).
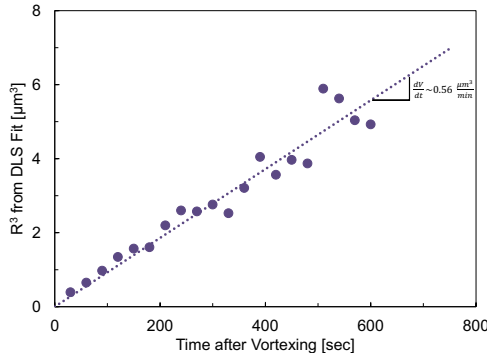

Figure S7: Ripening Rate Fit Example. Linear fit of droplet volume, calculated from the DLS hydrodynamic radius, versus time after vortex mixing. The 10mM r.u. and 4.5 M NaCl system gives a growth rate of $\dfrac{d\langle R\rangle^3}{dt} = 0.56 \ \dfrac{\mu m^3}{min}$.

Note 3.4   Concentration dependence

Increased total concentration of repeat units (PAA+PAH) at 1:1 mixing (constant salt concentration) speeds coacervate growth (Figure S8A). Meanwhile, increased total NaCl concentration at 1:1 mixing (constant polyelectrolyte concentration) has minimal impact on the coacervate growth in the microfluidic mixing device (Figure S8B). Note that the solubility limit of NaCl in pure water at at 25°C is about 5.4 M[6], so the data spans nearly the entire testable range of salt concentrations. At least the 0 M NaCl data should be aggregated in bulk according to our precipitate boundary observations in microfluidics (see Figure S11); however, since sizes reported here were extracted from images collected in the middle of the channel height, aggregated sediment was not observed.

The residence time on the microfluidic chip is approximately 75 seconds, during which time the droplet radius grows to around 0.8 to 1.5 μm depending on total composition. At 10 mM r.u. and 4.5 M NaCl, $\langle R\rangle \sim 0.8$ μm in microfluidics, so $\langle R\rangle^3 \sim 0.5$ μm^3. This size matches the drop size extracted from DLS (Figure S7) at comparable time.
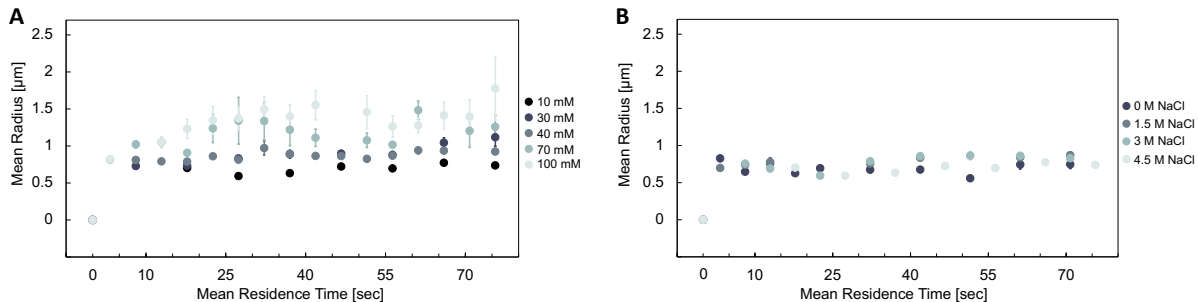
Figure S8: Growth of droplets in the microfluidic Y-junction. Data shown at (a) constant NaCl concentration (4.5 M NaCl) and various PAA + PAH repeat unit concentrations (b) constant polymer concentration (10 mM total PAA+PAH repeat units) at a constant flow rate (0.5 μL/min) through the microfluidic device. Mean droplet radius was extracted according to ESI Note 3.1.

Note 3.5   Further discussion

Since aggregates grow from individual droplets, it is important to consider the molecular-level transport responsible for droplet growth prior to colloidal aggregation. Prior studies have suggested that molecular-scale transport is an important factor in understanding the equilibration of individual PEC polymer chains. Both the order of mixing[7] and titration[8] are known to affect the thermodynamic pathway by which equilibrium is reached. Respectively, shifts in the phase boundary and mixing enthalpy were observed when polycation was added to an existing solution of polyanion, rather than in the reverse order. The microfluidic mixing used in this work represents the first study of coacervate drop formation and growth in a controlled flow environment, with mixing of PAA and PAH chains by cross-flow diffusion.

Our experiments reveal that the volume-averaged droplet radius grows as constant in $\frac{d<R>^3}{dt}$, which might suggest Ostwald Ripening [9] and the existence of nanoscale soluble moiety in the coacervating system. Past experimental work on coacervate phase separation supports molecular-level "aggregation" as a dominant mechanism for initial phase separation and growth, with individual polycation and polyanion chains pairing, then growing into PECs,[10, 11, 12, 13, 14] known as the Veis-Aranyi model in honor of the scientists who first proposed it.[15] While such polyanion-polycation pairs could feasibly act as the soluble moiety during growth by Ostwald Ripening, polyelectrolytes do not remain paired once in the coacervate phase. Thus, a kinetic step would be required for pair reformation during Ostwald Ripening, which makes this mechanism seem unfeasible. Further, Ostwald ripening is characterized by $\frac{dV}{dt} = \frac{8\gamma c_\infty v^2 D}{RT}$, where γ is the PEC surface tension, v is soluble moiety's solubility and c_∞ its molar volume, and RT is the molar thermal energy. Since γ, v, and c_∞ are all expected to be strong functions of salt for polyelectrolytes, it is unlikely that $\frac{dV}{dt} = \frac{8\gamma c_\infty v^2 D}{RT}$ independent of NaCl over nearly its entire range of solubility as observed.

Another possibility is that the growth mechanism of individual coacervate droplets is more strongly controlled by ϕ_d than by thermodynamic properties of a soluble moiety. In fact, constant $\frac{d<R>^3}{dt}$ could also correspond to a mechanism in which many tiny droplets continually aggregate onto existing droplets, analogous to Avrami-type crystal growth.[16, 17] Though the Avrami model results in sigmoidal extent of the new phase (slow start, faster increase, slow finish), a constant growth rate is observed during the period of faster size increase.[18] When applied to a suspension of spherical droplets, the Avrami model behaves like a non-dilute version of Ostwald Ripening (since both theories do not consider the droplet dissolution energetics necessary above some critical droplet size) but the mechanisms differ. Whereas Ostwald Ripening is driven by supersaturation-driven growth of the larger droplets only, individual drop size can also increase via coalescence in the Avrami model. Thus, an Avrami mechanism for growth of individual coacervate droplets does not require redissolution of a sticky-Rouse coacervate into individual soluble moieties, eliminating the other main mechanistic issues with Ostwald Ripening posed above. We postulate that the growth mechanism of small individual PEC droplets is therefore the *same as PEC*

growth at the larger, micron length scales at which we chiefly focused in this work. [1]

Note 4   PEC Sediment Growth and Properties

Note 4.1   Roughness of PEC sediment in microfluidics

To characterize microstructural roughness at various flow rates in microfluidics, at least three separate imaged regions fully contained inside the sediment formed at that flow rate were analyzed for their roughness. Regions were 30.42 µm x 30.42 µm (300x300 pixels, with pixel size 0.1014 µm). Each region was analyzed using a custom MATLAB™code. Micrographs were thresholded using the Otsu method, binarized, and inverted. Connected components were identified using 4-connectivity, and the resulting region with the largest number of pixels is identified. The Euler characteristic, χ, was calculated for this region and thus used to parameterize the roughness. This process is summarized graphically by an example in Figure S9. Since there is only a single 4-connected region in this case (the contiguous sediment), the absolute value of χ will depend on crop size within the sediment; but since the crop size is fixed, the relative value of χ can be compared across different samples.
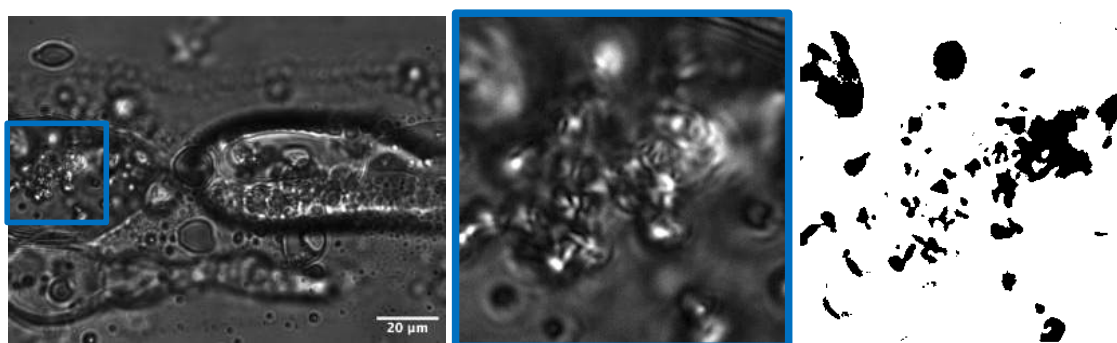

Figure S9: Example analysis of sediment formed at 5 µL/min flow rate and 90 mM total r.u. and 30 M NaCl. One subregion of this sediment is cropped (blue outline) and its associated black-and-white image used to calculate the Euler characteristic as a measure of overall sediment roughness. Here, there is a single 4-connected region (white) containing $\chi = 64$ holes.

Note 4.2   Rheology

To prepare samples for rheology, polyelectrolyte stock were mixed with salt stock solutions to a total volume of 10 mL, centrifuged at 2000 rpm for 30 minutes until complete phase separation was achieved, and supernatant was decanted. The PEC was scooped onto an AR-G2 stress-controlled rheometer (TA Instruments, New Castle, DE) with sandpaper applied to the center of the stage to maximize adhesion. Mineral oil was applied around the perimeter of each sample to prevent evaporation. Small-amplitude oscillatory shear (SAOS) measurements were conducted over the frequency range 0.01 - 500 rad/s in the linear viscoelastic region (2% shear strain) using an 8 mm parallel-plate geometry.

Our SAOS data at 0 M NaCl and 100 mM PAA+PAH r.u. (navy blue) is shifted and overlaid on the time-ionic strength superposition (TISS) master curve data (gray), reproduced with permission from Syed et al.[19] using their equation for the horizontal shift factor a_I and by fitting and interpolating their data for the vertical shift factor b_I applied to our composition (Figure S10). These TISS data published by Syed et al. use comparable molecular weights to our system: Syed et al. estimate the degree of polymerization (N) for their polymers as $N_{PAA} = 158$ and $N_{PAH} = 160$, whereas for our polymers $N_{PAA} = 160$ and $N_{PAH} = 187$. We attribute the slight vertical offset in our data relative to their TISS master curve to these modest differences in N, our use of interpolation to calculate the vertical shift factor, and/or to small discrepancies in sample preparation (e.g., evaporation). Our PAA-PAH complexes show viscous-dominant behavior ($G'' > G'$ for all measured frequencies) at equilibrium, consistent with

---

[1]It might seem to contradict the Avrami model that, for mechanistic arguments, we assumed droplets at short l are ∼1 μm no matter what flow rate (Figure S8B), and that droplet size remains ∼1 μm until it impacts a larger PEC particle in pipette and vortex mixing. Strictly, this assumption is only validated for the average droplet at microfluidic-accessible flow rates. Regardless, our mechanistic arguments easily generalize to the case in which droplet size has broad distribution.
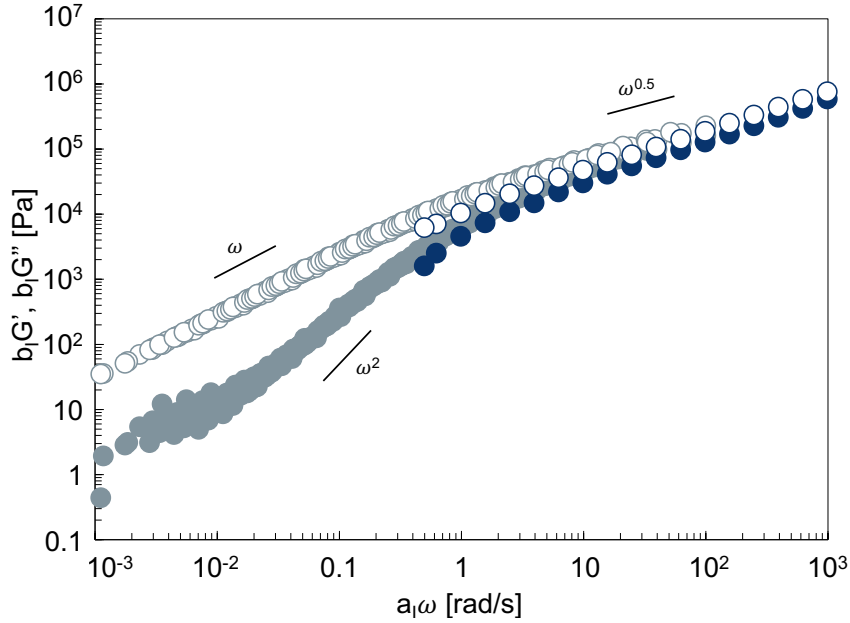
Figure S10: Linear viscoelastic behavior (SAOS) of PAA-PAH dense phase at equilibrium. The universal TISS master curve (gray) and shift factors were obtained from Syed et al.[19] The overlaid data (navy blue) represents a sample of our coacervate at 100 mM r.u. and 0 M NaCl with 1:1 mol:mol PAH:PAA. Loss modulus (open circles) exceeds storage modulus (closed circles) across compositions, demonstrating viscoelastic liquid dynamics even at salt-free conditions for this coacervate chemistry. Power-law slopes reveal low-frequency terminal relaxation ($G'' \sim \omega$ and $G' \sim \omega^2$) and high-frequency behavior ($G'' \sim \omega^{0.5}$) consistent with Rouse-like relaxation.

others' extensive characterization at higher salt of the equilibrium rheology of the PAA-PAH chemistry at the same chain lengths.[1, 19] Together with the measurements of Syed et al., the dynamic response demonstrates Rouse-like relaxation dynamics: the loss modulus G'' (open circles) goes as ω^1 in the low-frequency limit and $\omega^{0.5}$ in the high-frequency limit; and the storage modulus G' (closed circles) goes as ω^2 at low frequency.

Note 4.3   Microfluidic mixing

Microstructural observation in microfluidic flow reveal aggregated structures at larger PAA+PAH repeat unit concentrations and lower NaCl (Figure S11). At lower polyelectrolyte concentration and higher NaCl, the sedimented structures have less (or completely lack) internal structure and flow along the bottom of the channel as dense liquids in the direction of the mixing flow.
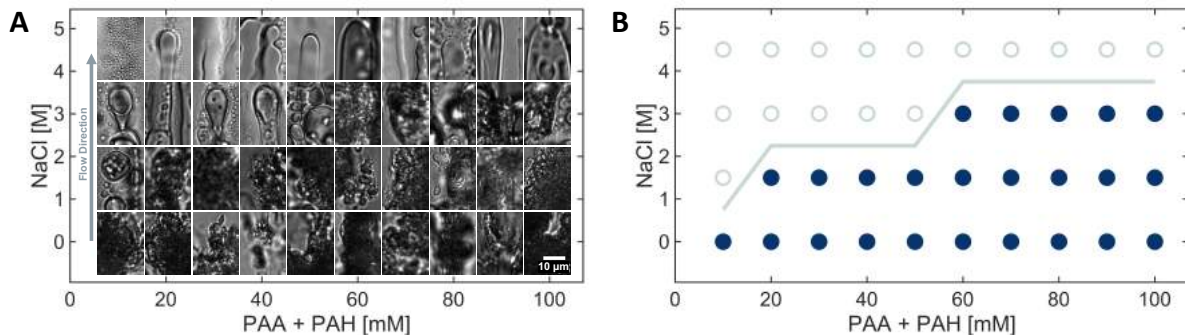

Figure S11: Growth of PEC sediment in microfluidics at a fixed 25 μL/min flow rate results in different microstructures as a function of total salt and PAA+PAH repeat unit concentration. (a) Micrographs of PEC sediment at various mixed compositions. (b) Microstructural coacervate-precipitate boundary, with filled symbols indicating conditions where aggregated microstructures are observed.

Note 4.4   Concentration dependence

Samples prepared by pipetting 100 μL of PEC emulsion into a glass-bottomed 96-well plate and left to phase separate quiescently were coarsened by gravitational sedimentation. Images were taken across the entire bottom surface of the wells after gravitational coarsening and tiled. The raw tiled images are shown at a variety of compositions in Figure S12.
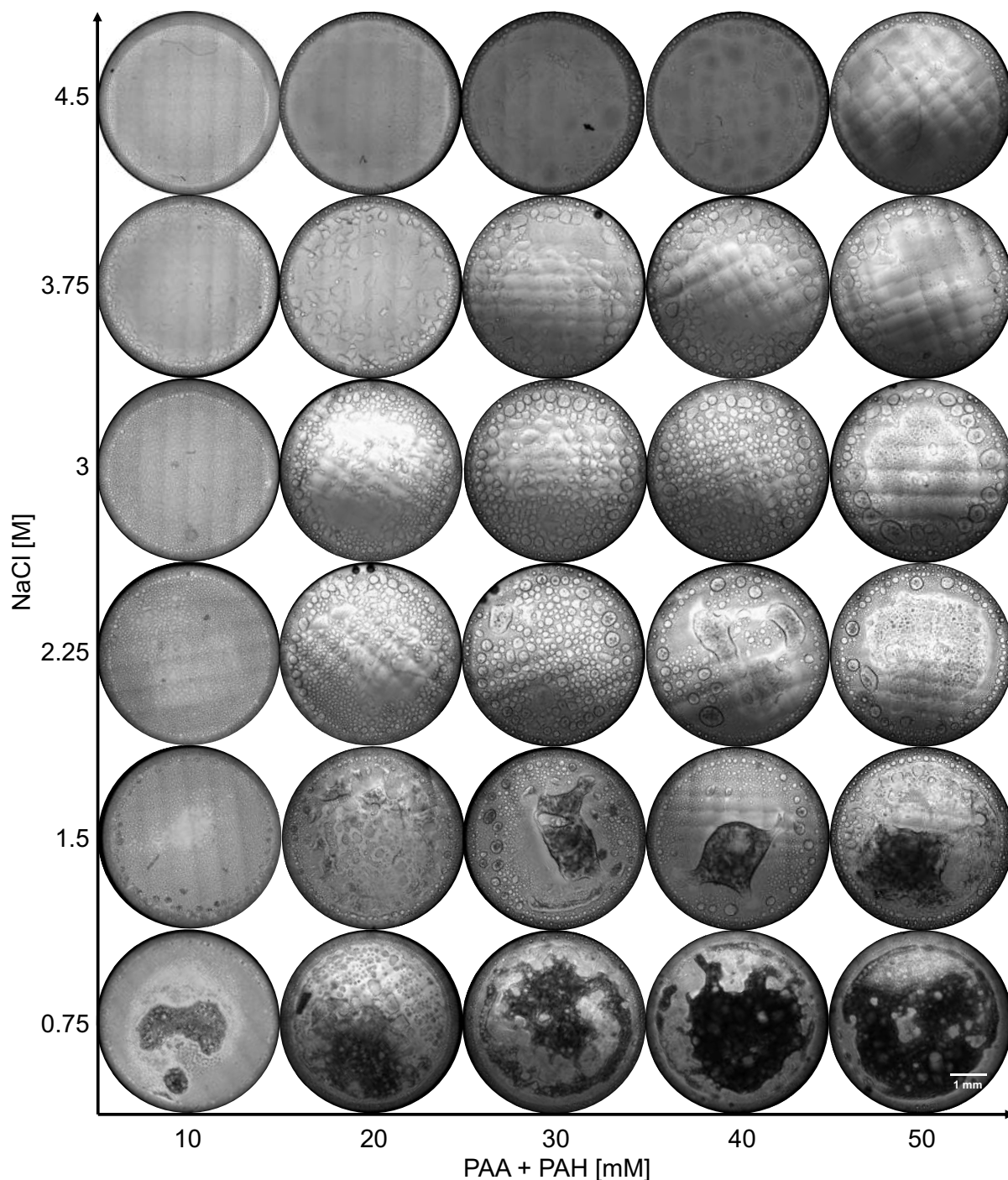

Figure S12: Tiled images of pipette-mixed PAA/PAH emulsions transferred to a 96-well plate and allowed to sediment for 2 days at a variety of compositions.

Limitations in the dynamic range of the microscope across the wide field of view required for image tiling across multiple wells obviated the use of the same algorithm to quantitatively characterize microstructural roughness as in Figure S9. We instead compare the fraction of white pixels in binarized versions of the tiled well images (Figure S13A) as a qualitative proxy for roughness. The images in Figure S13A were

generated using Auto *Local* Thresholding in Fiji (Phansalkar method with radius 15 and parameters 1, 2 = 0). Local thresholding was necessary to minimize the effect of dynamic range differences across each well and highlight the local structure within each tile. Wells with larger white-fractions generally correspond to less rough sediment in the wells, since more attenuation occurs where internal interfaces are more abundant in the sediment. Results are available in Figure S13B, which reveals that microstructural roughness generally increases toward higher polymer concentration and lower total salt content. Please note that the roughness results from this analysis should be interpreted qualitatively due to the intrinsic challenges in analyzing the intensity of tiled images.
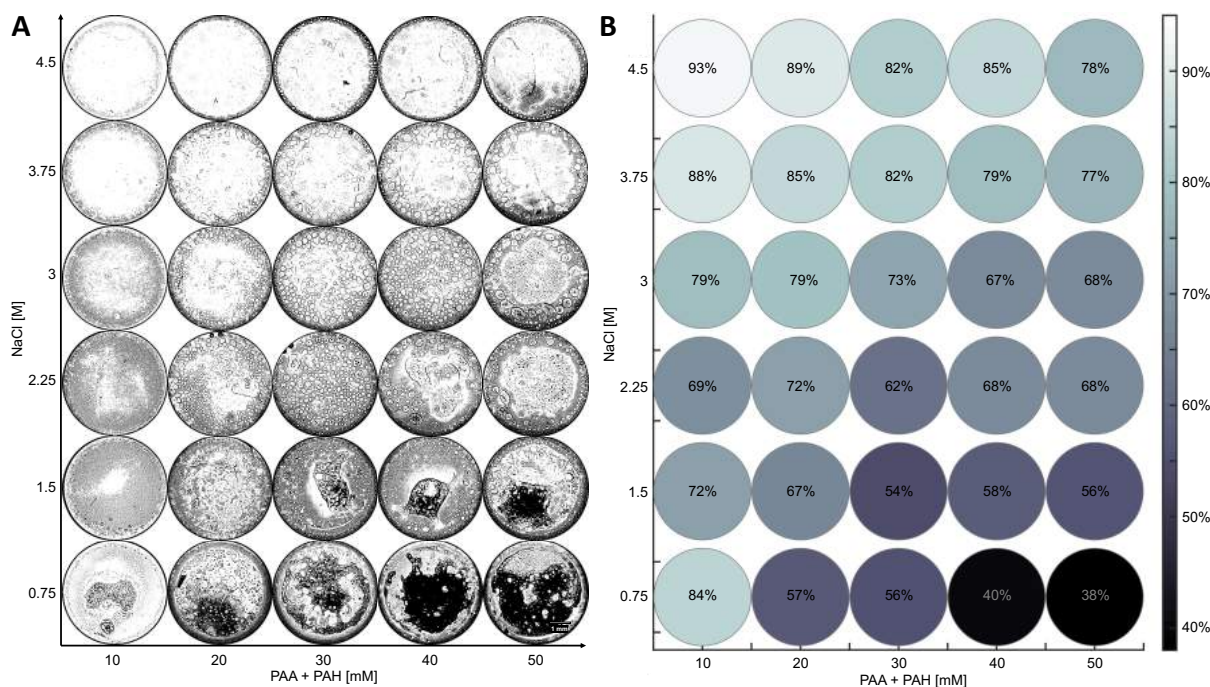

Figure S13: Quantification of concentration-dependent roughness in tiled images of PAA/PAH emulsions sedimented in a 96-well plate for 2 days at a variety of compositions. (a) Binarized versions of tiled images used for quantification; methodology described above. (b) Fraction of white pixels in binarized tiled image of each well, as a function of total polymer and salt composition.

Note 4.5   Dilute-phase inclusions

Note 4.5.1   Fluorescent sample preparation

Fluorescent labelling of the dense phase in gravitationally-sedimented samples is achieved through addition of colloidal yellow-green polystyrene-carboxylate spheres ($2a = 1$ μm Polysciences, Warrington, PA) added during preparation of the PECs. The particles were pre-washed in deionized water, then combined with the Milli-Q water during mixing to maintain a particle volume fraction of ~ 0.01 vol % in the dense phase across compositions. We previously showed that these particles partition into the dense phase of the PAA/PAH chemistry and introduce negligible charge to the system at 0.01 vol %.[1] The PECs were grown by gravitational sedimentation in a 96-well plate and imaged after 48 hours.

Note 4.5.2   Fluorescent imaging

Fluorescent samples were imaged using the Zeiss Axio Observer 7 microscope and a $10\times$ objective (NA = 0.3, magnification = 590 nm/pixel), the same setup used for image tiling of the 96-well plate in brightfield. Fluorescence mode was achieved using a Colibri 7 light source and standard GFP filter set. Micrographs were brightness- and contrast-adjusted for clarity.
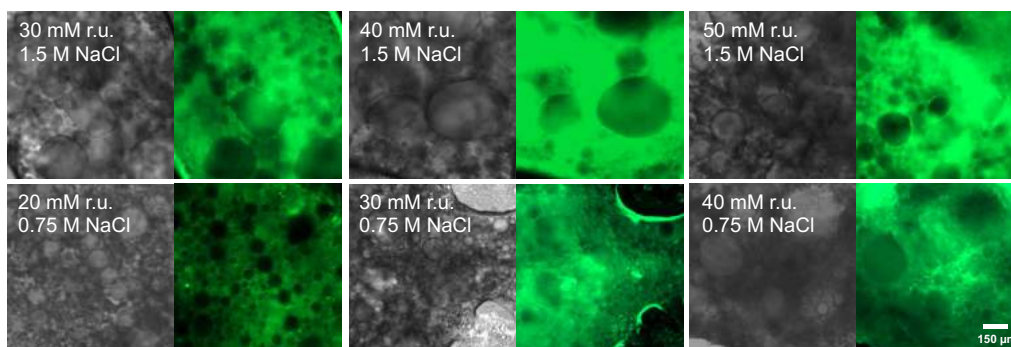
Figure S14: Fluorescence labelling of the dense phase reveals dilute phase droplets trapped within the PEC sediment. Brightfield and fluorescence micrographs are shown at various indicated compositions.

Note 5   Aging of PEC Microstructure

Note 5.1   Aging of gravitationally-sedimented samples

Dilute-phase inclusions significantly coarsen over 8 days at most compositions in gravitationally-sedimented samples. This section compares PEC structure in the 96-well plate on the 10th day at all compositions presented above (Note 4.4), which are shown on the 2nd day. In other words, the micrographs in Figures S15 and S16 show the qualitative progression of microstructural relaxation 8 days after Figures S12, S13, and S14. Note that Figure S16B was generated with binarized versions of the tiled images using the same methodology as Figure S13B. For these images, the window and level were automatically adjusted in Fiji prior to binarizing the image so that each micrograph contains the same range of pixel intensity (Day 2 data were already properly adjusted). Figure S16A shows the tiled well-plate images after level adjustment.
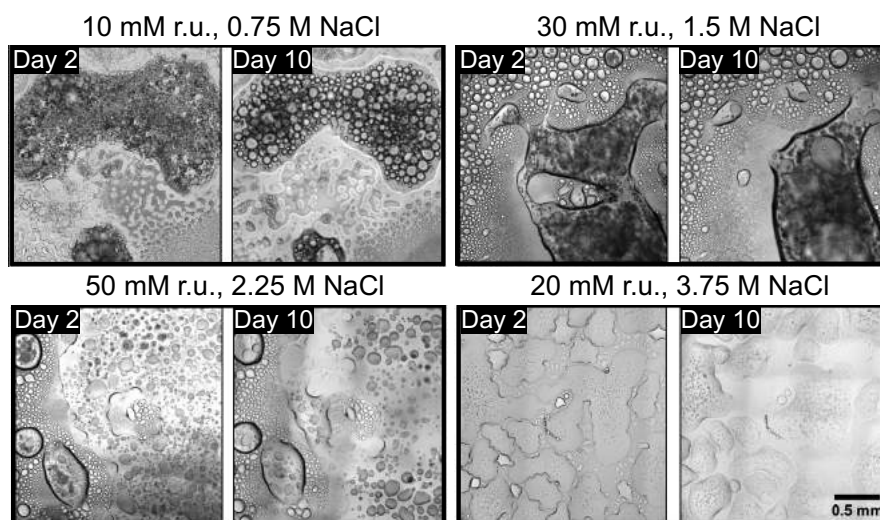

Figure S15: Direct comparison of micrographs of gravitationally-sedimented PECs on the 2nd and 10th day after mixing, at various selected compositions. Trapped dilute-phase droplets within the surrounding dense phase PEC grow in size between Days 2 and 10 at all compositions.
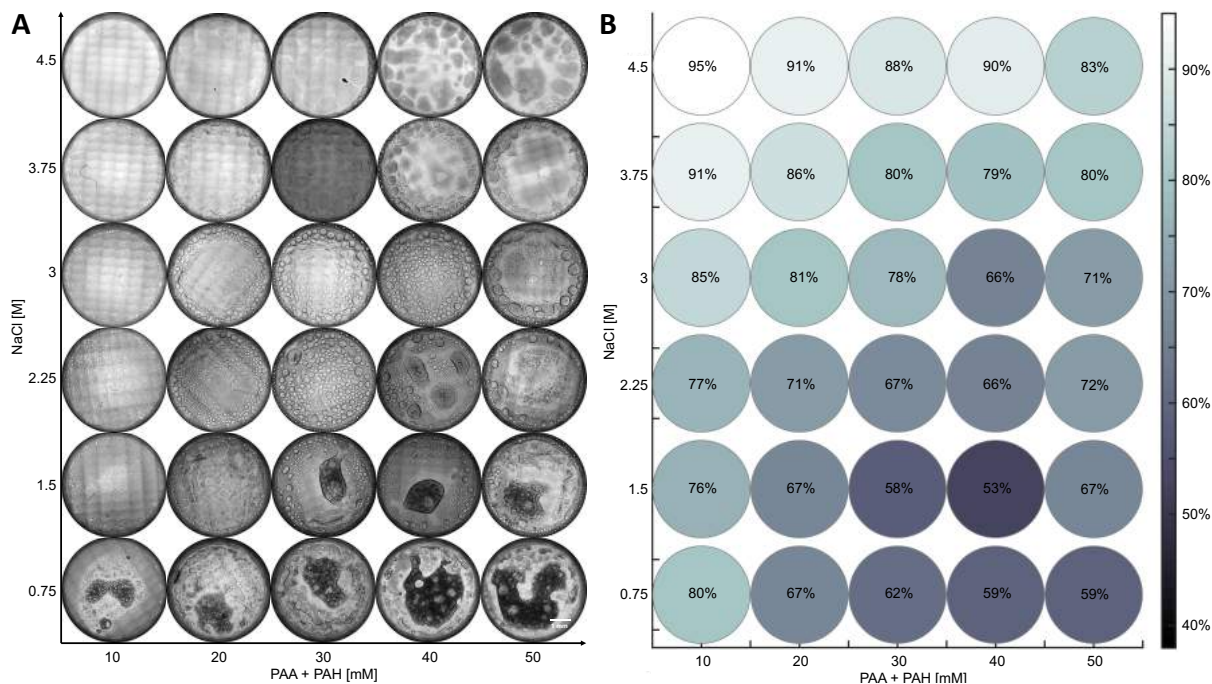
Figure S16: PAA/PAH emulsions sedimented in a 96-well plate on the 10th day. (a) Tiled images of samples after 10 days at all tested compositions. (b) Fraction of white pixels in binarized tiled image of each well in (a), as a function of total polymer and salt composition.

Note 5.2 Aging of aggregates

After mixing by pipette with specified additional number of seconds of vortex mixing (Section 5.3.3), 100 μL of solution was transferred to a 96-well plate and imaged every 30 seconds using a Zeiss Axio Observer 7 microscope (0.293 μm/pixel) as described in Section 5.4.1. Video data begins around 2.5 minutes after mixing is complete, with a frame collected every 30 seconds, and videos are manually cropped around individual aggregate structures. Using a custom MATLAB™code, cropped videos are thresholded using the Otsu method, binarized, and inverted. To identify the largest structure in the video, connected components are identified using 4-connectivity, and the resulting region with the largest number of pixels (i.e., the relaxing aggregate) is identified. The Euler characteristic χ was calculated according to the methodology described in ESI Note 4.1. Using this method, the relaxing aggregate is the largest structure in each video identified by the 4-connectivity. As a result, the time-dependent change in χ is not affected by features external to each aggregate that change during the video, such as sedimentation of nearby droplets, or the crop size. When the filled area of the largest region changed less than 2% in 90 seconds, the structure was considered relaxed. Prior to this timepoint, the timecourse of χ is fit to the model function $\chi = b_1 e^{-t/b_2}$ where t is the experimental time after mixing is complete and $\tau_{relax} = \frac{1}{b_2}$, the characteristic aggregate relaxation time.

Various correlations between τ_{relax} and other variables are shown in Figure S17 and the Pearson product-moment correlation coefficient r and corresponding p-value are listed for each. Aside from vortex mixing time (Figure S17H), τ_{relax} is uncorrelated to all variables except standard error of fit (Figure S17D)—since the larger τ_{relax} have larger error at the same (uncorrelated) percent error—and the number of observations (Figure S17E). The observation cutoff occurs when the area starts changing minimally, so samples that relax faster show more change between each frame and take more observations to reach the cutoff. This dependence of τ_{relax} on the number of observations does not account for the dependence of τ_{relax} on vortex time, because vortex time and number of observations are uncorrelated (Figure S17J).
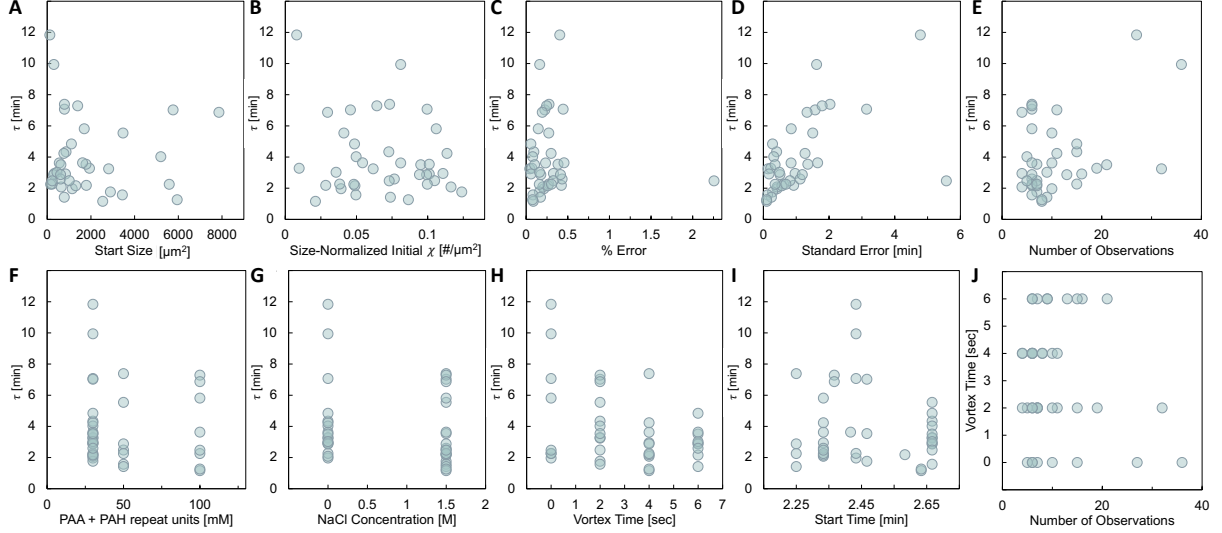
Figure S17: Correlations of τ_{relax} and other variables in the aggregate aging and fitting experiment. (a) τ_{relax} is not correlated to the initial size (filled area) of the aggregate (r = -0.003, p = 0.986). (b) τ_{relax} is not correlated to the initial size-normalized χ of the aggregate (r = -0.183, p = 0.264). (c) τ_{relax} is not correlated to the percent error of fit (r = -0.020, p = 0.904). (d) τ_{relax} is correlated to standard error of fit (r = 0.579, p = 0.0001). (e) τ_{relax} is correlated to the number of observations (r = 0.428, p = 0.006). (f) τ_{relax} is not correlated to the overall polymer concentration (r = -0.044, p = 0.159). (g) τ_{relax} is not correlated to the overall salt concentration (r = 0.076, p = 0.707). (h) τ_{relax} is correlated to the vortex time used to prepare the sample (r = -0.389, p = 0.014). (i) τ_{relax} is not correlated to the time after mixing at which the video was started (r = -0.137, p = 0.404). (j) Vortex time is not correlated to the number of observations (r = -0.169, p = 0.304).

Note 5.3 Comparison of τ_{relax} to various timescales

τ_{rheol} for the PAA-PAH system is estimated using data published by Syed et al.[19] As introduced in ESI Note 4.2, our SAOS data shifts onto the published PAA-PAH time-ionic strength superposition (TISS) master curve they provided for similar chain lengths, using shift factors from their work (Figure S10). This enables us to extract longest relaxation time using their data, which should be comparable to τ_{rheol}, the relevant timescale for liquid-like flow relaxation of our material.

We select the composition 30 mM r.u. and 0 M, as shown in Figure 6 as a representative test case to extract τ_{rheol}. Using their conversion factor from wt % to M units of polyelectrolyte concentration, k = 0.053 M/wt%, we obtain that 30 mM r.u. is 0.566 wt% polyelectrolyte. Ionic strength is given by I [M] = $C_s + k\alpha C_p$, where $C_s = 0$ and C_p are the weight percentage of the salt and polymer in solution. α is the charge fraction, which is approximately 1 at pH 6.5. Thus, ionic strength is I = 0.03 M. The horizontal shift factor is given by $a_I \sim \exp(-4.74\ I^{0.5})$; we find the exponential prefactor to be 22.17 via fitting the data from Figure 4b of Syed et al.[19] At I = 0.03 M, a_I = 9.75. Finally, we extrapolate a power-law fit of the data in the terminal flow regime where G'' goes as ω to find the longest relaxation time. In particular, G'' goes as $\omega^{0.5}$ in the high-frequency regime, and the crossover point between the power-law extrapolation of the high- and low-frequency regimes give a reasonable approximation for τ_{rheol}. This estimation is shown graphically in Figure S18. We estimate the crossover where $20206(a_I\omega_{cross})^{0.9382}$ = $19489(a_I\omega_{cross})^{0.5413}$, giving ω_{cross} = 0.094 rad/s. The estimated viscoelastic relaxation time is then $1/\omega_{cross} = \tau_{rheol}$ = 10.6 s. This is about an order of magnitude smaller than the τ_{relax} we find (100s of seconds).

Estimation of the visco- and inertio- capillary times are as follows. An order of magnitude estimate of the PAA-PAH PEC viscosity is μ = 5 Pa s = 5 kg/(m s), as given in our previous rheology measurements on this system at 100 mM r.u. and 4.5 M NaCl.[1] The density ρ is calculated using that the volume fraction of PAA-PAH PEC at pH 6.5 is around 0.4, that the approximate densities of each component are $\rho_{polymer}$ = 1.3308 g/mL, ρ_{salt} = 2.16 g/mL, and ρ_{water} = 1.00 g/mL at 20 C, and the assumption that density of polymer and salt are the same in the bulk and solution state as used by Li et al.[4] Since

the salt volume fraction is around 0, then the water volume fraction is around 0.6, and the density can be calculated as $\rho = 0.4(1.3308) + 0.6(1) = 1.132$ g/mL ≈ 1100 kg/m^3. We estimate initial drop size as about 0.5 μm. Across varied coacervate chemistries, surface tension γ has been typically measured to be order of magnitude 1 mJ/m^2 (0.001 ks/s^2). Thus, the visco-capillary time $\tau_{vc} = \frac{\mu R}{\gamma}$ can be calculated as order 0.001 s, and the inertio-capillary time is $\tau_{ic} = \sqrt{\frac{\rho R^3}{\gamma}} \approx 3.7\text{e-}7 \sim 1\text{e-}7$ s.
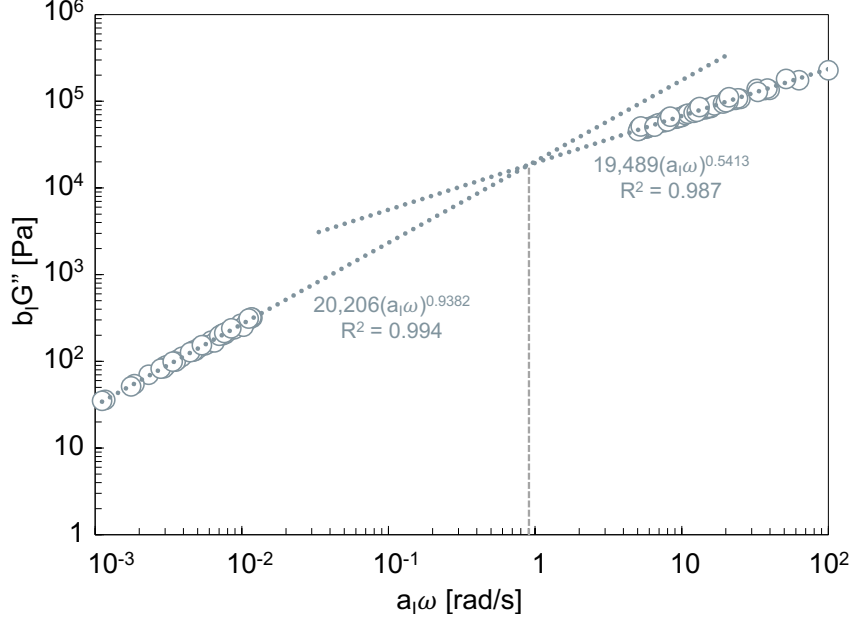

Figure S18: Power-law fit of the universal TISS curve loss modulus data (Figure S10) above $a_I\omega = 5$ rad/s and below $a_I\omega = 0.012$ rad/s. Intermediate frequency data was removed, showing the high frequency (G'' $\sim \omega^{0.5}$) and low frequency terminal relaxation (G'' $\sim \omega$) limits, and their fits and extrapolation. The crossover predicts the estimated terminal relaxation timescale, which corresponds to $a_I\omega = 0.9$ rad/s.

Note 5.3.1   Calculation of [dimensionless] τ* regime

The Ohnesorge number, Oh, relates viscosity, surface tension, and density as Oh $= \frac{\mu}{\sqrt{\rho R \gamma}}$, and has recently been used to show qualitative similarity between coalescence, spreading, and pinching of droplets.[20] Using the values from the prior section, Oh ≈ 6700 for our system. Using Oh, Varma et al. define a dimensionless time regime calculated as τ* $= \sqrt{\frac{Oh\,\tau_{rheol}}{\tau_{ic}}} \approx 8.1 \times 10^5$.

Note 6   Re and Pe estimations

Note 6.1   Relevant dimensions, timescales, and flow rates

Microfluidic channel dimensions are measured using profilometry of the 3D-printed mold, with a Keyence VHX-5000 microscope. Pipette tip and microcentrifuge tube dimensions were measured with a vernier caliper. Linear flow rates are calculated as though they were steady-state; in reality there are significant effects on the flow from start-up and, in the case of pipette mixing, eddies formed from imposed changes in flow direction.

Microfluidic channel:

Width: 432 ± 8 μm

Height: 38 ± 3 μm

Hydraulic diameter: $\frac{4A}{P} = 69.8$ μm, with A cross-sectional area, P perimeter. So $\mathbf{L_{micro}} = \mathbf{70}$ μm

Volumetric flow rates range from 0.5 - 0.25 μL/min

Pipette tip:

D_{tip}, the tip diameter at the narrowest opening, is $\approx$ 1.1 mm. Call **$L_{\text{pipette}} = 500\ \mu\text{m}$**

The average volume of added 1 M r.u. PAH stock solution is around $V_{\text{avg}} = 10$ uL

It takes about 0.4 s on average to dispense the contents of the pipette tip

Microcentrifuge tube:

D_{max} of the tube is around 8 mm; **$L_{\text{tube}} = 4000\ \mu\text{m}$**

Rotational velocity at some radius r is $v_{\text{r}}(\text{r}) = 3200$ rpm * 2πr

Using these dimensions and timescales, we can estimate the following linear flow rates in microfluidics, for pipette mixing, and for vortex mixing, respectively:

$u_{\text{micro}} = 1000$*(flow rate in $[\mu\text{L/min}]$), which ranges from **$u_{\text{micro}} = 5000 - 25000\ \mu\text{m/sec}$**

$u_{\text{pipette}} = \frac{V_{avg}}{\pi (L_{pipette})^2 * 0.4s} =$ **$u_{\text{pipette}} = 32000\ \mu\text{m/sec}$**

$u_{\text{vortex}} = \frac{\int_0^{2\pi} \int_0^{L_{tube}} v_r(r)\, dr d\theta}{(L_{tube})^2}$, or around **$u_{\text{vortex}} = 10^6\ \mu\text{m/sec}$**

Note 6.2   Reynolds numbers

These droplet Reynolds number (Re_{d}) estimates assume that the dilute phase has fluid properties (density ρ and kinematic viscosity μ) of pure water at 25°C.

$Re_{\text{micro}} = \frac{\rho u_{micro} L_{micro}}{\mu}$, which ranges from $Re_{\text{micro}} = 0.035 - 1.74$ as u_{micro} increases   Order 1

$Re_{\text{pipette}} = \frac{\rho u_{pipette} L_{pipette}}{\mu} = 15.9$ Order 10

$Re_{\text{vortex}} = \frac{\rho u_{vortex} L_{tubee}}{\mu} = 3988$ in transition to turbulence, Order 1000

Note 6.3   Péclet estimates

The Péclet number for mass transfer (Pe_{d}) describes the ratio between advective and diffusive transport rates. In other words, as Pe_{d} increases, flow effects are likely to contribute more to the system behavior. These estimates assume that the diffusing species are spherical droplets with radii of order 0.5μm in all mixing approaches, consistent with microscopy for microfluidic mixing. This is equivalent to assuming that droplet growth happens much more slowly than the colloidal aggregation or coalescence described herein under various mixing conditions: the time at observation is only seconds to several minutes after initial droplet formation. Additionally, the Stokes-Einstein diffusivity of the diffusing and advected particles is: **$D_{\text{drop}} = 0.49\ \mu\text{m}^2/\text{s}$**, assuming 25°C and the dynamic viscosity of pure water. The following are Pe_{d} estimates in microfluidic, pipette, and vortex mixing:

$Pe_{\text{micro}} = \frac{u_{micro} L_{micro}}{D_{\text{drop}}}$, which ranges from $Pe_{\text{micro}} = 0.07 - 3.6*10^6$ as u_{micro} increases

$Pe_{\text{pipette}} = \frac{u_{pipette} L_{pipette}}{D_{\text{drop}}} = 3.3*10^7$

$Pe_{\text{vortex}} = \frac{u_{vortex} L_{tube}}{D_{\text{drop}}} = 8.2*10^9$.

Comparing these values gives the following ratios: $\frac{Pe_{vortex}}{Pe_{pipette}} \approx 250$ and $\frac{Pe_{vortex}}{Pe_{micro}} \approx 50{,}000$

References

[1] Y. Luo, M. Gu, C. E. Edwards, M. T. Valentine, and M. E. Helgeson, "High-throughput microscopy to determine morphology, microrheology, and phase boundaries applied to phase separating coacervates," *Soft Matter*, vol. 18, no. 15, pp. 3063–3075, 2022.

[2] R. Chollakup, J. B. Beck, K. Dirnberger, M. Tirrell, and C. D. Eisenbach, "Polyelectrolyte molecular weight and salt effects on the phase behavior and coacervation of aqueous solutions of poly (acrylic acid) sodium salt and poly (allylamine) hydrochloride," *Macromolecules*, vol. 46, no. 6, pp. 2376–2390, 2013. 74.

[3] R. Chollakup, W. Smitthipong, C. D. Eisenbach, and M. Tirrell, "Phase behavior and coacervation of aqueous poly (acrylic acid)- poly (allylamine) solutions," *Macromolecules*, vol. 43, no. 5, pp. 2518–2528, 2010. 72.

[4] L. Li, S. Srivastava, S. Meng, J. M. Ting, and M. V. Tirrell, "Effects of non-electrostatic intermolecular interactions on the phase behavior of ph-sensitive polyelectrolyte complexes," *Macromolecules*, vol. 53, no. 18, pp. 7835–7844, 2020. 30.

[5] M. Nguyen, N. Sherck, K. Shen, C. E. Edwards, B. Yoo, S. Kohler, J. C. Speros, M. E. Helgeson, K. T. Delaney, M. S. Shell, *et al.*, "Predicting polyelectrolyte coacervation from a molecularly informed field-theoretic model," *Macromolecules*, 2022.

[6] D. L. Perry, *Handbook of inorganic compounds*. CRC press, 2016.

[7] W. C. B. McTigue, E. Voke, L.-W. Chang, and S. L. Perry, "The benefit of poor mixing: kinetics of coacervation," *Physical Chemistry Chemical Physics*, vol. 22, no. 36, pp. 20643–20657, 2020. 53.

[8] L. Vitorazi, N. Ould-Moussa, S. Sekar, J. Fresnais, W. Loh, J.-P. Chapel, and J.-F. Berret, "Evidence of a two-step process and pathway dependency in the thermodynamics of poly (diallyldimethylammonium chloride)/poly (sodium acrylate) complexation," *Soft Matter*, vol. 10, no. 47, pp. 9496–9505, 2014.

[9] P. Taylor, "Ostwald ripening in emulsions," *Advances in colloid and interface science*, vol. 75, no. 2, pp. 107–163, 1998.

[10] V. A. Kabanov and A. B. Zezin, "Soluble interpolymeric complexes as a new class of synthetic polyelectrolytes," *Pure and Applied Chemistry*, vol. 56, no. 3, pp. 343–354, 1984. 62.

[11] H. T. Oyama and C. W. Frank, "Structure of the polyion complex between poly (sodium p-styrene sulfonate) and poly (diallyl dimethyl ammonium chloride)," *Journal of Polymer Science Part B: Polymer Physics*, vol. 24, no. 8, pp. 1813–1821, 1986. 68.

[12] A. I. Petrov, A. A. Antipov, and G. B. Sukhorukov, "Base- acid equilibria in polyelectrolyte systems: From weak polyelectrolytes to interpolyelectrolyte complexes and multilayered polyelectrolyte shells," *Macromolecules*, vol. 36, no. 26, pp. 10079–10086, 2003.

[13] D. Priftis and M. Tirrell, "Phase behaviour and complex coacervation of aqueous polypeptide solutions," *Soft Matter*, vol. 8, no. 36, pp. 9396–9405, 2012. 73.

[14] D. Priftis, K. Megley, N. Laugel, and M. Tirrell, "Complex coacervation of poly (ethyleneimine)/polypeptide aqueous solutions: Thermodynamic and rheological characterization," *Journal of colloid and interface science*, vol. 398, pp. 39–50, 2013.

[15] A. Veis and C. Aranyi, "Phase separation in polyelectrolyte systems. i. complex coacervates of gelatin," *The Journal of Physical Chemistry*, vol. 64, no. 9, pp. 1203–1210, 1960.

[16] V. Špillar and D. Dolejš, "Calculation of time-dependent nucleation and growth rates from quan-

titative textural data: inversion of crystal size distribution," *Journal of Petrology*, vol. 54, no. 5, pp. 913–931, 2013.

[17] T. Vetter, M. Iggland, D. R. Ochsenbein, F. S. Hanseler, and M. Mazzotti, "Modeling nucleation, growth, and ostwald ripening in crystallization processes: a comparison between population balance and kinetic rate equation," *Crystal Growth & Design*, vol. 13, no. 11, pp. 4890–4905, 2013.

[18] M. Avrami, "Kinetics of phase change. ii transformation-time relations for random distribution of nuclei," *The Journal of chemical physics*, vol. 8, no. 2, pp. 212–224, 1940.

[19] V. M. Syed and S. Srivastava, "Time–ionic strength superposition: A unified description of chain relaxation dynamics in polyelectrolyte complexes," *ACS Macro Letters*, vol. 9, no. 7, pp. 1067–1073, 2020. 40.

[20] M. A. Fardin, M. Hautefeuille, and V. Sharma, "Spreading, pinching, and coalescence: the ohnesorge units," *Soft Matter*, vol. 18, no. 17, pp. 3291–3303, 2022.